Supporting Information

Probing LaMO$_3$ metal and oxygen partial density of states using X-ray emission, absorption, and photoelectron spectroscopy

Wesley T. Hong,[*,†] *Kelsey A. Stoerzinger,*[†] *Brian Moritz,*[§,‖] *Thomas P. Devereaux,*[§] *Wanli Yang,*[⊥] *Yang Shao-Horn*[*,†,‡]

[†] Department of Materials Science and Engineering,

[‡] Department of Mechanical Engineering, Massachusetts Institute of Technology, Cambridge, MA 02139, USA

[§] Stanford Institute for Materials and Energy Sciences, SLAC National Accelerator Laboratory, Menlo Park, CA 94025, USA

[‖] Department of Physics and Astrophysics, University of North Dakota, Grand Forks, ND 58202, USA

[⊥] Advanced Light Source, Lawrence Berkeley National Laboratory, Berkeley, CA 94720, USA

Index **Page**

X-ray diffraction

All samples used in this study were characterized by X-ray diffraction (PANalytical) to determine phase purity (Fig. S1). Lattice parameters were determined by profile fitting (FullProf) (Table S1), in good agreement with those reported previously.[1-5] $LaFeO_3$, $LaMnO_{3+\delta}$, and $LaCoO_3$ were all phase pure within the experimental resolution of the diffractometer. The $LaCrO_3$ sample showed a small impurity of La_2O_3 (~8%) and the $LaNiO_{3-\delta}$ contained a trace amount of NiO (~2%), denoted by (*) in Fig. S1. It should be noted that, the contribution of the impurities to the X-ray spectroscopic data in these systems is believed to be negligible due to the low impurity concentration, which is supported by the strong agreement of our XAS spectra (both O *K*-edge and TM *L*-edge) with those of phase-pure oxides reported previously.[6-8]

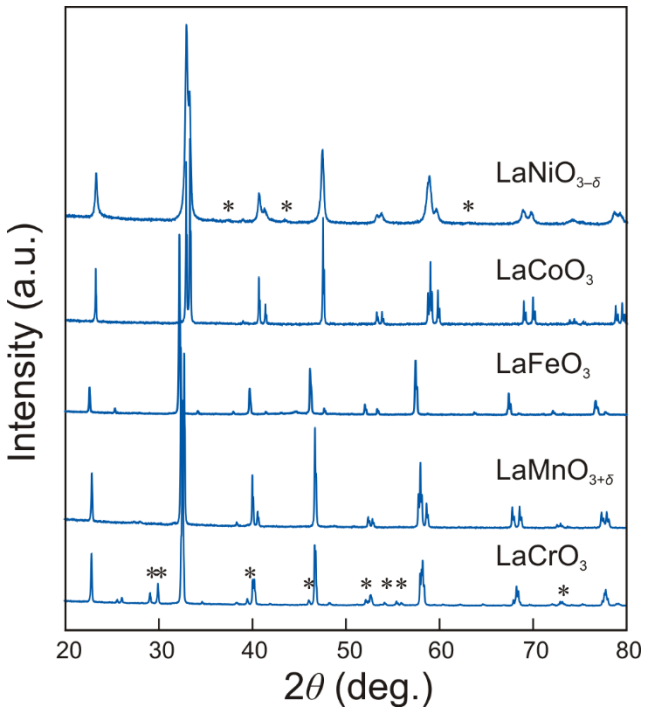

Figure S1. X-ray diffraction patterns using a Cu *Kα* source for prepared La*M*O_3 oxides (*M* = Cr, Mn, Fe, Co, Ni). (*) indicates a small La_2O_3 impurity (~8%) in the $LaCrO_3$ and NiO impurity (~2%) in the $LaNiO_{2.98}$. All other samples show phase purity within the experimental resolution of the diffractometer.

Compound	Symmetry	*a* (Å)	*b* (Å)	*c* (Å)	*α*	*β*	*γ*
$LaCrO_3$	*Pnma*	5.575	7.760	5.483	90º	90º	90º
$LaMnO_{3.08}$	$R\bar{3}c$	5.528	5.528	13.340	90º	90º	120º
$LaFeO_3$	*Pnma*	5.566	7.853	5.554	90º	90º	90º
$LaCoO_3$	$R\bar{3}c$	5.443	5.443	13.092	90º	90º	120º
$LaNiO_{2.98}$	$R\bar{3}c$	5.456	5.456	13.165	90º	90º	120º

Table S1. La*M*O_3 (*M* = Cr, Mn, Fe, Co, Ni) lattice parameters obtained by profile fitting of the X-ray diffraction patterns.

O *K*-edge and TM *L*-edge XAS spectra

All spectra were normalized to the absorption background both before the absorption edge and 40 eV above the absorption edge (Fig. S2). The O *K*-edge spectra are in good agreement with those published previously.[9, 10] The TM $L_{2,3}$ spectra confirm the formal 3+ TM oxidation state for all of the samples.[7, 11-13] $LaNiO_{2.98}$ shows a prominent difference for the TEY and TFY spectra. The $LaNiO_{2.98}$ spectral features in TEY are identical to those observed previously in phase-pure samples,[8] and the difference between TEY and TFY spectra can be attributed to overlap with the La M_4-edge, where the contribution from the La absorption is significantly reduced in TFY due to the weak fluorescence at the *M*-edge. The poor Cr *L*-edge TFY data of $LaCrO_3$ is attributed to strong self-absorption due to its proximity to the O *K*-edge.

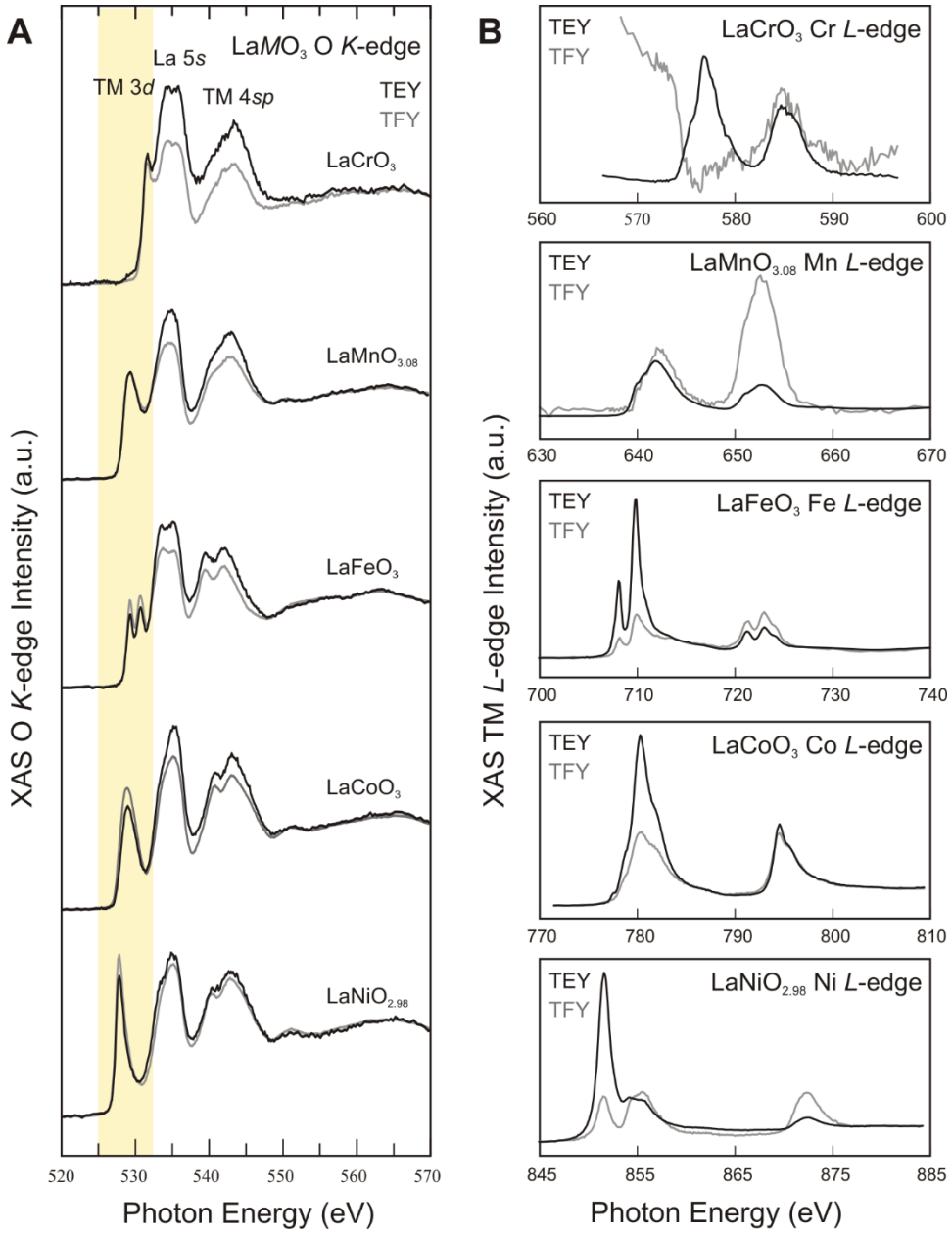

Figure S2. (A) X-ray absorption spectra of O *K* for the La*M*O$_3$ oxides collected in total electron yield (TEY, black) and total fluorescence yield (TFY, gray). (B) X-ray absorption spectra of TM $L_{2,3}$ for the La*M*O$_3$ oxides collected in total electron yield (TEY, black) and total fluorescence yield (TFY, gray). The TM $L_{2,3}$ of all oxides confirm the formal 3+ oxidation state. Substantial self-absorption effects in the TFY are apparent in $LaCrO_3$ and $LaMnO_{3.08}$ due to the proximity of the Cr and Mn *L*-edges to the O *K*-edge. The Ni $L_{2,3}$ spectrum overlaps with the La M_4-edge;[8] the contribution from the La absorption is significantly reduced in TFY due to the weak fluorescence at the *M*-edge. All spectra are normalized to the backgrounds both before the absorption edge and 40 eV above the absorption edge.

Smoothing and differentiation of XES spectra

For each XES spectrum, the data was first smoothed using a fast Fourier transform (FFT) filter. By assessing the frequency dependence of the spectral intensities, it was apparent that experimental noise primarily contributes at frequencies beyond 0.4 eV^{-1}. This was therefore selected as the filter cut-off frequency. A representative spectral smoothing ($LaNiO_{2.98}$) is depicted in Fig. S3, illustrating preservation of the spectral features while substantially improving the signal-to-noise for analysis.

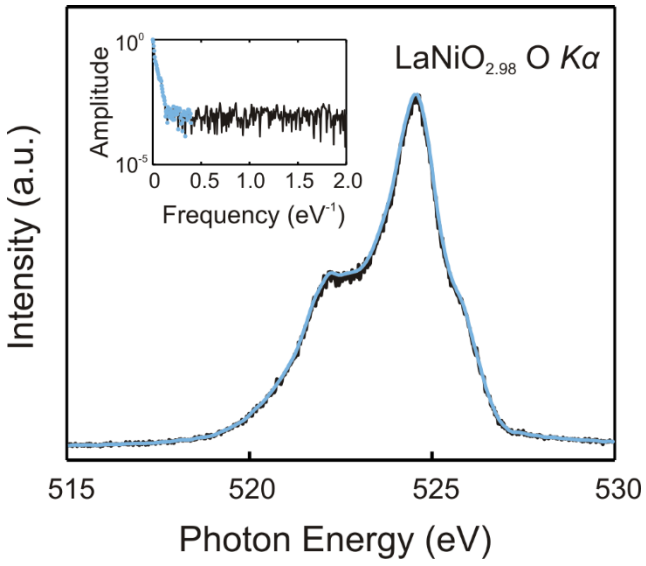

Figure S3. Representative spectral smoothing shown for $LaNiO_{2.98}$ O *Kα*. The smoothed data (blue line) shows good fidelity with the raw data (black line). A cut-off frequency of 0.4 eV^{-1} was used based on the amplitude dependence in the frequency domain (inset; blue line illustrates selected frequencies).

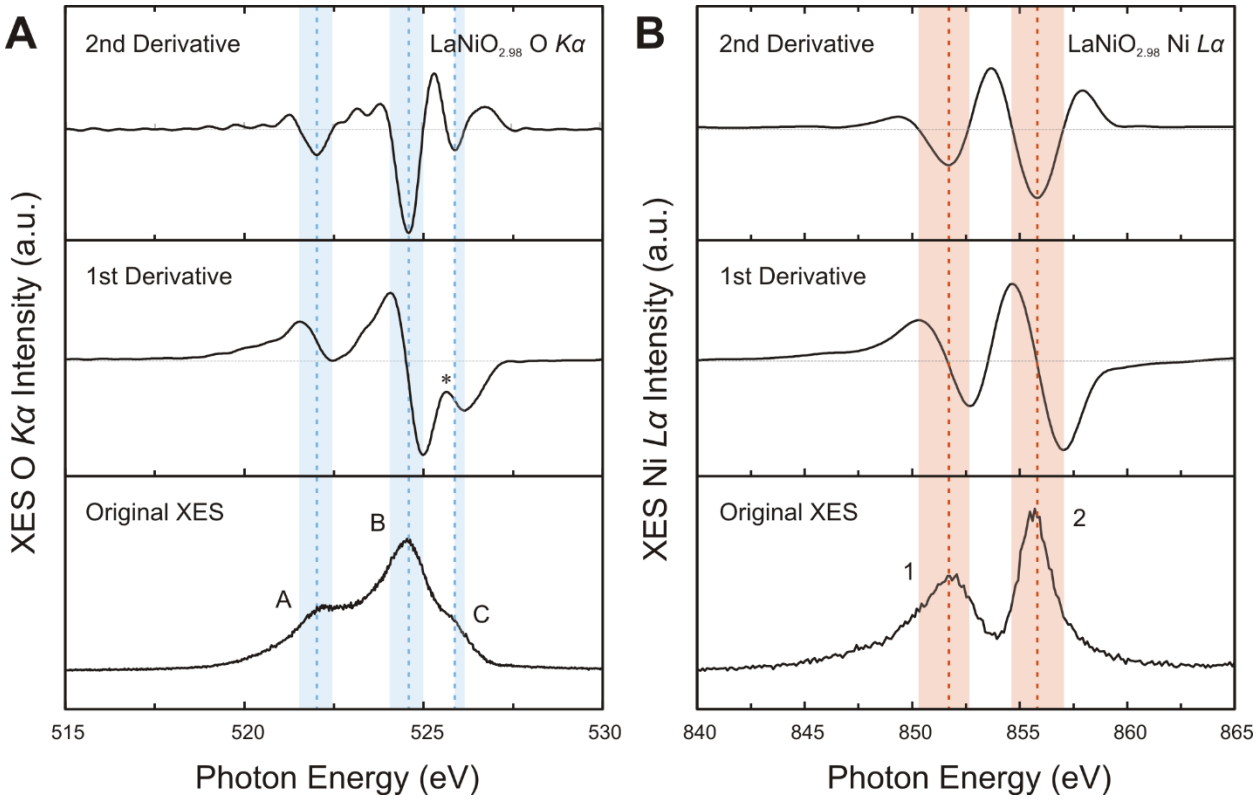

Figure S4. (A) Representative smoothed differentiation shown for $LaNiO_{2.98}$ O *Kα*. (B) Representative smoothed differentiation shown for $LaNiO_{2.98}$ TM *Lα*. Positions for spectral features observable in the raw data were quantified using minima in the second derivative (dashed lines) and estimates for the standard error were obtained using the adjacent local maxima and minima in the first derivative (shaded region). In cases where the standard error bounds were poorly defined for a given feature (i.e. the first derivative had a local maximum that was negative or minimum that was positive, such as for peak C in the O *Kα* spectrum – starred), the average standard error obtained from the other features in the spectrum was used.

In the limit that the electronic bandwidths and Lorentzian broadening associated with the intrinsic core-hole lifetime are relatively small compared to the instrumental broadening, bands in the spectra approach a Gaussian limit. Motivated by the properties of Gaussian distributions, we used minima in the second derivative to quantify the positions of features visible in the raw spectra, and took the nearest local maximum and minimum in the first derivative to estimate the standard error (requiring that the maximum be positive and the minimum be negative). Smooth differentiation

was accomplished by the additional application of a Savitsky-Golay smoothing algorithm, generating a reliable differential curve with good signal-to-noise. This form of processing by smoothing and differentiation is commonly employed in analyzing FTIR spectra.[14] Representative figures of the raw and smoothed XES data, first derivative, and second derivative ($LaNiO_{2.98}$) are illustrated in Fig. S4, where the dashed lines indicate the spectral feature positions and the shaded regions indicate the standard error. It is clear that this method is particularly useful for assigning energies to evident but convoluted features, such as feature C in the O *Kα* spectrum. In general, it was found that the standard error for different, well-defined features within the same spectrum did not deviate substantially. Consequently, in cases where the standard error bounds were poorly defined for a given feature (i.e. the first derivative had a local maximum that was negative or minimum that was positive, such as for peak C in the O *Kα* spectrum), the average standard error obtained from the other features in the spectrum was used.

Alignment of XES spectra using XPS core-hole binding energies

Our method of aligning the XES spectra with XPS valence band measurements to obtain the partial DOS involves aligning the O *Kα* and TM *Lα* spectra using the hybridization features, taking the superposition, and then aligning the lowest energy peak of the superposition with the lowest energy XPS valence band feature. Thus, we first establish the physical interpretation of the spectra in order to obtain the offsets between the XES and XPS valence band. In doing so, features between spectra that have a common physical origin are fixed to have identical energy, providing an intrinsically robust method of obtaining the partial DOS on the binding energy scale. In contrast, the conventional approach uses core-level binding energies to first estimate the offset between the XES and XPS valence band in order to provide physical interpretation of the spectra. Therefore, this form of alignment relies on an assumed relation between the XES and XPS valence band energy scales.

The offsets needed to redefine the oxygen and transition metal XES energy scales to the binding energy scale ($E_{\text{binding}} = E_{\text{offset}} - E_{\text{XES}}$) using our approach can be compared to the conventional method of taking the corresponding XPS core-level binding energies (the O 1*s* and TM $2p_{3/2}$) as the offset (Table S2). The values of the XPS core-level binding energies of the perovskites in this study are consistent with values that have been reported previously in literature[15-20] and are systematically larger than the offsets obtained from our method by as much as 2 eV.

Compound	O 1*s* BE (eV)	Actual O *Kα* Offset (eV)	TM 2$p_{3/2}$ BE (eV)	Actual TM *Lα* Offset (eV)
$LaCrO_3$	528.4	527.4	575.5	573.7
$LaMnO_{3.08}$	529.2	528.7	641.8	640.9
$LaFeO_3$	529.1	528.4	709.9	709.1
$LaCoO_3$	528.6	527.6	779.7	777.7
$LaNiO_{2.98}$	528.2	527.0	*	854.0

Table S2. Comparison of XPS core-level binding energies with offsets obtained from aligning the superposed XES spectra with XPS valence band data. *The position of the Ni 2$p_{3/2}$ could not be determined due to overlap with the La 3$d_{3/2}$.

Fig. S5 illustrates the XES spectra offset using the core-level binding energies (the Ni *Lα* was offset by the same amount determined using the hybridization features because the Ni 2$p_{3/2}$ overlaps strongly with the La 3$d_{3/2}$). Using this method, the hybridization features in the O *Kα* and TM *Lα* are not consistently aligned, and the relative positions of features in the superposed spectra (dashed gray) does not generally agree with the positions of the XPS valence band features. This can be contrasted with our method, shown in Fig. 3 of the main text and reproduced below.

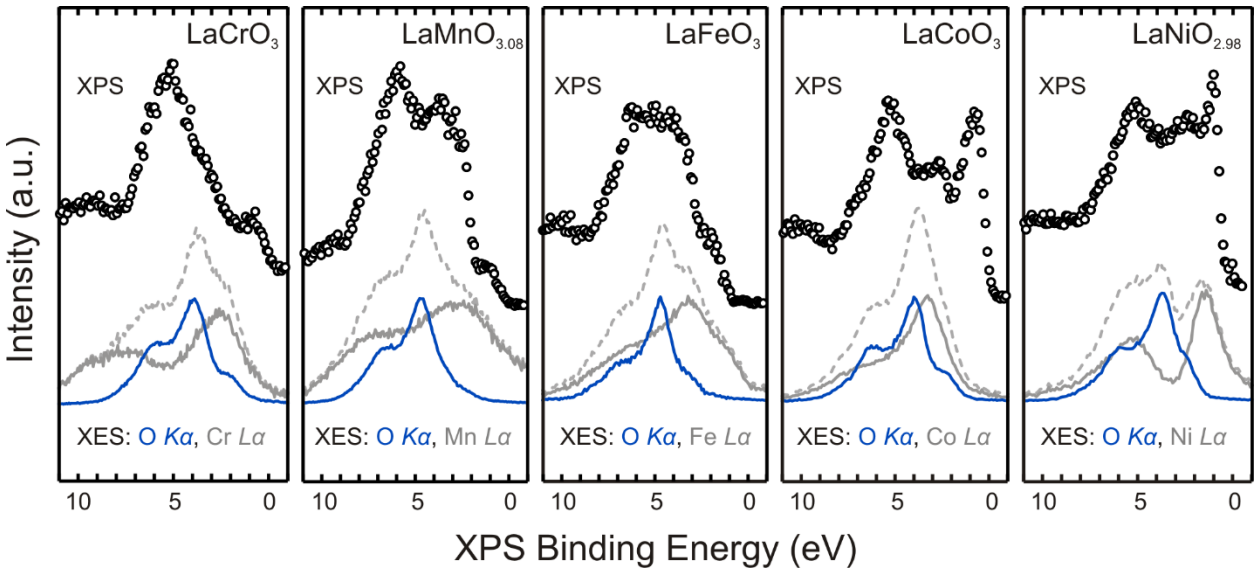

Figure S5. Alignment of XES spectra with XPS spectra for the LaMO$_3$ oxides. The O $K\alpha$ spectra were offset by the O 1s binding energies and the TM $L\alpha$ were offset by the TM 2$p_{3/2}$ binding energies (values provided in Table S2). XES spectra were arbitrarily normalized to the maximum peak intensity. Using this method, the hybridization features in the O $K\alpha$ and TM $L\alpha$ are not consistently aligned, and the relative positions of features in the superposed spectra (dashed gray) does not generally agree with the positions of the XPS valence band features.

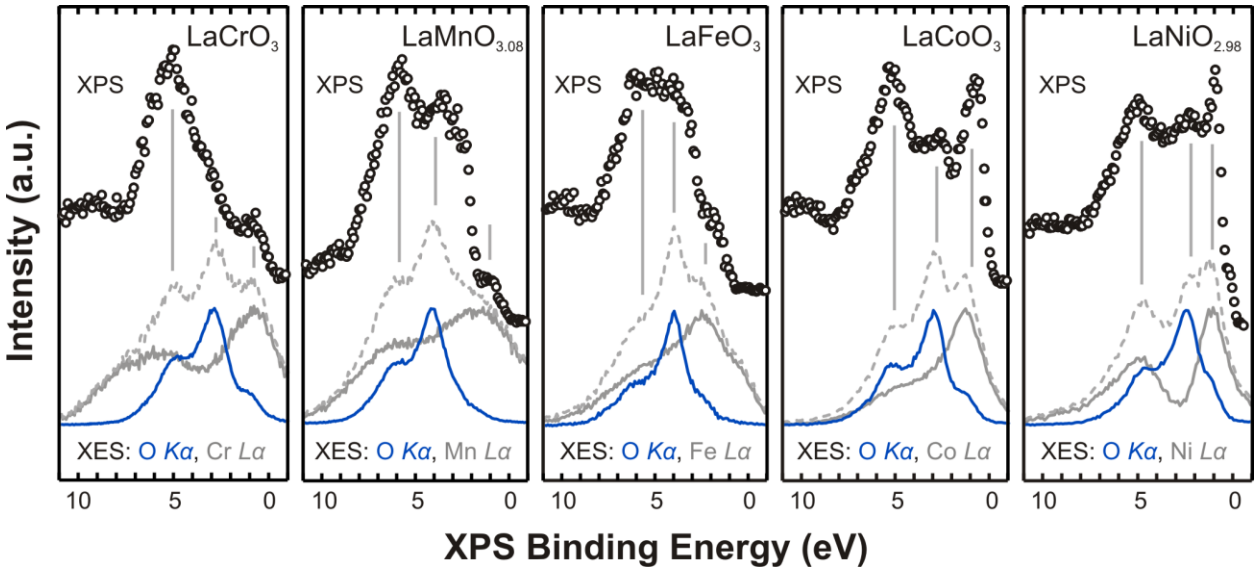

Figure 3. (reproduced from main text) Alignment of XES spectra with XPS spectra for the LaMO$_3$ oxides. The superposed XES spectra (dashed gray) were aligned to the XPS spectra using the lowest binding energy peak. Light gray lines illustrate good agreement for the relative peak positions in the superposed emission spectra with the valence band photoemission data, indicating

that the alignment of the emission spectra captures the true partial DOS. XES spectra were arbitrarily normalized to the maximum peak intensity.

Supporting Information References

(1) Tezuka, K.; Hinatsu, Y.; Nakamura, M.; Inami, T.; Shimojo, Y.; Morii, Y. Magnetic and Neutron Diffraction Study on Perovskites $La_{1-x}Sr_xCrO_3$. *J. Solid State Chem.* **1998**, *141*, 404-410.

(2) van Roosmalen, J. A. M.; Cordfunke, E. H. P. The Defect Chemistry of $LaMnO_{3\pm\delta}$ - 4: Defect Model for $LaMnO_{3+\delta}$. *J. Solid State Chem.* **1994**, *110*, 109-112.

(3) Dann, S. E.; Currie, D. B.; Weller, M. T.; Thomas, M. F.; Al-Rawwas, A. D. The Effect of Oxygen Stoichiometry on Phase Relations and Structure in the System $La_{1-x}Sr_xFeO_{3-\delta}$ ($0 < x < 1$, $0 < \delta < 0.5$). *J. Solid State Chem.* **1994**, *109*, 134-144.

(4) Radaelli, P.; Cheong, S. W. Structural phenomena associated with the spin-state transition in $LaCoO_3$. *Phys. Rev. B*. **2002**, *66*.

(5) García-Muñoz, J.; Rodríguez-Carvajal, J.; Lacorre, P.; Torrance, J. Neutron-diffraction study of $RNiO_3$ (R=La,Pr,Nd,Sm): Electronically induced structural changes across the metal-insulator transition. *Phys. Rev. B*. **1992**, *46*, 4414-4425.

(6) Ong, K.; Blaha, P.; Wu, P. Origin of the light green color and electronic ground state of $LaCrO_3$. *Phys. Rev. B*. **2008**, *77*.

(7) Sarma, D. D.; Maiti, K.; Vescovo, E.; Carbone, C.; Eberhardt, W.; Rader, O.; Gudat, W. Investigation of hole-doped insulating $La_{1-x}Sr_xCrO_3$ by soft-x-ray absorption spectroscopy. *Phys. Rev. B*. **1996**, *53*, 13369-13373.

(8) Medarde, M.; Fontaine, A.; García-Muñoz, J.; Rodríguez-Carvajal, J.; de Santis, M.; Sacchi, M.; Rossi, G.; Lacorre, P. $RNiO_3$ perovskites (R=Pr,Nd): Nickel valence and the metal-insulator transition investigated by x-ray-absorption spectroscopy. *Phys. Rev. B*. **1992**, *46*, 14975-14984.

(9) Sarma, D.; Shanthi, N.; Mahadevan, P. Electronic excitation spectra from *ab initio* band-structure results for La*M*O_3 (*M* = Cr, Mn, Fe, Co, Ni). *Phys. Rev. B*. **1996**, *54*, 1622-1628.

(10) Suntivich, J.; Hong, W. T.; Lee, Y. L.; Rondinelli, J. M.; Yang, W.; Goodenough, J. B.; Dabrowski, B.; Freeland, J. W.; Shao-Horn, Y. Estimating Hybridization of Transition Metal and Oxygen States in Perovskites from O *K*-edge X-ray Absorption Spectroscopy. *J. Phys. Chem. C*. **2014**, *118*, 1856-1863.

(11) Cramer, S. P.; deGroot, F. M. F.; Ma, Y.; Chen, C. T.; Sette, F.; Kipke, C. A.; Eichhorn, D. M.; McKee, V.; Mullins, O. C.; Fuggle, J. C. Ligand Field Strengths and Oxidation States from Manganese L-Edge Spectroscopy. *J. Am. Chem. Soc.* **1991**, *113*, 7937-7940.

(12) Hu, Z.; Wu, H.; Haverkort, M.; Hsieh, H.; Lin, H.; Lorenz, T.; Baier, J.; Reichl, A.; Bonn, I.; Felser, C.*; et al.* Different Look at the Spin State of Co^{3+} Ions in a CoO_5 Pyramidal Coordination. *Phys. Rev. Lett.* **2004**, *92*.

(13) Abbate, M.; de Groot, F. M. F.; Fuggle, J. C.; Strebel, O.; Lopez, F.; Domke, M.; Kaindl, G.; Sawatzky, G. A.; Takano, M.; Takeda, Y.*; et al.* Controlled-valence properties of $La_{1-x}Sr_xFeO_3$ and $La_{1-x}Sr_xMnO_3$ studied by soft-x-ray absorption spectroscopy. *Phys. Rev. B*. **1992**, *46*, 4511-4519.

(14) Smith, B. C., *Fundamentals of Fourier Transform Infrared Spectroscopy*. Taylor and Francis Group, LLC: Boca Raton, FL, 2011.

(15) Vasquez, R. P. X-ray photoemisson measurements of $La_{1-x}Ca_xCoO_3$ ($x = 0, 0.5$). *Phys. Rev. B*. **1996**, *54*, 14938-14941.
(16) Zhao, X.; Yang, Q.; Cui, J. XPS study of surface absorbed oxygen of ABO_3 mixed oxides. *Journal of Rare Earths*. **2008**, *26*, 511-514.
(17) Estemirova, S. H.; Fetisov, A. V.; Fetisov, V. B. X-ray Photoelectron Spectroscopy Study of the Electronic Structure of $La_{1-x}Ca_xMnO_{3+\delta}$ Solid Solutions. *J. Appl. Spectrosc.* **2009**, *76*, 394-401.
(18) Sarma, D. D. Electron Spectroscopic Data of $La_{1-x}Sr_xMnO_3$ and $La_{1-x}Sr_xCoO_3$. *Surf Sci Spectra*. **1999**, *6*, 274.
(19) Liu, X.; Su, W.; Lu, Z. Study on valence state and electrical conductivity of $La_{1-x}Ca_xCrO_3$. *J. Phys. Chem. Solids*. **2001**, *62*, 1919-1921.
(20) Li, X.; Zhang, H.; Liu, X.; Li, S.; Zhao, M. XPS study on O(1s) and Fe(2p) for nanocrystalline composite oxide $LaFeO_3$ with the perovskite structure. *Mater. Chem. Phys.* **1994**, *38*, 355-362.